The use of complex compounds in chemical vapour deposition

2004 J. Phys.: Condens. Matter 16 S531

(http://iopscience.iop.org/0953-8984/16/5/010)

INSTITUTE OF PHYSICS PUBLISHING JOURNAL OF PHYSICS: CONDENSED MATTER

J. Phys.: Condens. Matter **16** (2004) S531–S552 PII: S0953-8984(04)69428-8

The use of complex compounds in chemical vapour deposition

Valentin Bessergenev

Department of Physics, FCT, University of Algarve, Campus de Gambelas, 8000 Faro, Portugal

E-mail: vbess@ualg.pt

Received 23 September 2003
Published 23 January 2004
Online at stacks.iop.org/JPhysCM/16/S531 (DOI: 10.1088/0953-8984/16/5/010)

Abstract

During the last decade volatile metal complexes have been employed in the synthesis of oxide and sulfide thin films on an increasing scale. In this contribution some experimental details of the chemical vapour deposition technique and results of the use of complex compounds are discussed. The peculiarities of growth kinetics are demonstrated with several recent results.

1. Introduction

The chemical vapour deposition (CVD) technique is a vapour deposition technique based on homogeneous or heterogeneous chemical reactions. Depending on conditions such as vapour pressure and temperature, both types of reaction or only one of them takes place during the deposition process. These processes employ various gaseous, liquid and solid chemicals as sources of elements (precursors) of which the film is to be formed. Table 1 shows the modifications of CVD processes that are frequently used in practice.

A large variety of single-crystalline, polycrystalline and amorphous thin films of metals, dielectrics and semiconductors of III–V and II–VI groups were prepared by the CVD technique.

The CVD deposition results from a set of phenomena occurring in the gas phase and/or at the surface of the substrate [1]. These phenomena in general can be divided into the following steps: homogeneous reactions in the gas state; diffusion of reactants to the substrate surface; adsorption of reactants at the surface; heterogeneous chemical reaction on the surface of the substrate; surface diffusion; lattice incorporation; desorption of by-products from the surface.

In this paper the metallo-organic chemical vapour deposition (MOCVD) technique and, particularly, a relatively new branch of this technique—the use of complex compounds (CC CVD) for oxide and sulfide thin film preparation will be discussed.

The paper is organised as follows. Section 2 gives some typical features of the MOCVD technique for pyrite (FeS_2), alumina (Al_2O_3) and titanium dioxide (TiO_2) thin film synthesis. Section 3 is focused on complex compounds and some peculiarities of the complex compounds

0953-8984/04/050531+22$30.00

Table 1. CVD techniques.

Technique	Source of energy promoting the reaction	Typical parameters for different CVD techniques		
		P (Torr)	T (°C)	C = Prec./Carr.Gas
CVD[a]	Thermal	10^{-5}–760	200–600	0.001–1
MOCVD[b]	Thermal	10^{-3}–760	200–600	0.001–1
PECVD[c]	Plasma	10^{-2}–10	100–400	0.01–1
PCVD[d]	Light	10^{-3}–10	100–400	0.01–1

[a] CVD—thermally activated CVD.
[b] MOCVD—metallo-organic CVD uses compounds containing metals bonded to organic radicals.
[c] PECVD—plasma-enhanced CVD uses a plasma to ionise and dissociate gases.
[d] PCVD—photo-assisted CVD uses light to initiate reaction or to enhance the reaction rate.

chemical vapour deposition (CC CVD) technique as well as on the discussion of properties of the thin films obtained. The paper is summarised in section 4.

2. MOCVD technique

The MOCVD reactors that are in use today are generally of one of two types.

(1) A cylindrical cold-wall quartz reactor chamber using a resistance-heated Mo or graphite susceptor.
(2) A rectangular hot-wall quartz chamber using RF or lamp heating of a graphite susceptor which can employ rotation of individual substrates to improve uniformity of the films.

As typical examples of MOCVD technique applications, iron pyrite (FeS_2) [2], Al_2O_3 [3] and TiO_2 [4] thin film preparation are discussed. These materials were chosen because of their practical importance.

2.1. Pyrite (FeS_2) synthesis

Iron pyrite has attracted interest with respect to its possible applicability as an absorber material for thin film solar cells. The main reasons for the interest concerning solar energy conversion are the suitable energy band gap (E_g = 0.8–0.95 eV), the very high absorption coefficient ($\sim 10^5$ cm^{-1}) and its composition of abundant, cheap and non-toxic elements.

The MOCVD system used in [2] comprises a vertical cold-wall reactor with resistance heater, the process gas supply, the pumping system and the gas-wasting unit (figure 1). The reactor was made of a 400 mm long quartz tube (inner diameter 60 mm) which was connected to metal flanges on both sides. The temperature of the resistance heated graphite substrate holder was measured by two Ni/CrNi thermocouples and controlled by the temperature controller.

Iron pentacarbonyl (IPC), which has only a low thermal stability, was used as the iron precursor, and di-*tert*-butyldisulfide (TBDS) was chosen as the sulfur precursor [2]. The structural formulae and some properties of the precursors are shown in table 2. The vapour pressure of IPC is much higher (39 mbar at 25 °C) than that of TBDS (1 mbar) [2]. Therefore in addition to a low IPC bubbler temperature (−17 °C) a dilution stage for the iron line was used as is usual for doping precursors in commercial MOCVD systems. In the dilution process it is necessary to work with high S/Fe ratios in the gas phase to avoid any $Fe_{1-x}S$ phase formation.

The process gas supply consisted of two lines for the liquid precursors. The carrier gas flows were controlled with mass flow controllers. The pressure in the reactor was controlled

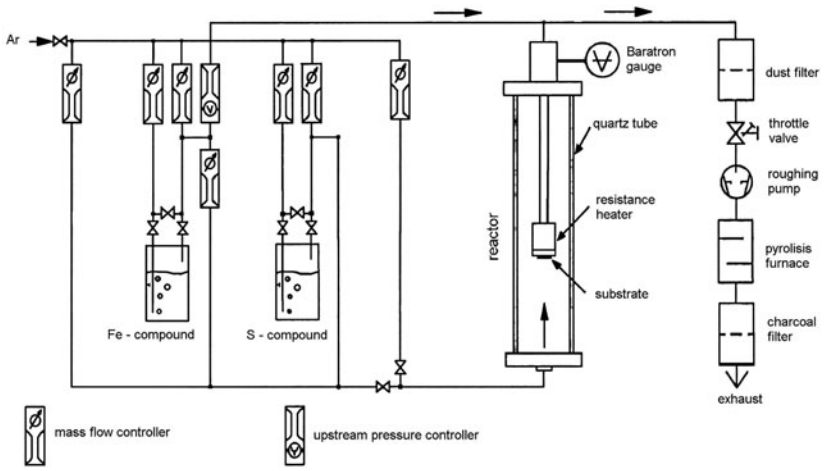

Figure 1. Schematic diagram of the MOCVD system including the vertical reactor and the process gas supply.

by a throttle valve. The exhaust gases were pyrolized at 800 °C in an oxygen atmosphere. The partial pressures of the precursors in the reactor can be estimated for IPC according to the equation $\log(P) = B - A/T$, with P in Torr, $B = 8.514$ and $A = 2105$ [1], and for TBDS by extrapolating known values at relatively high temperature (>60 °C) to the temperature of the bubbler (5–50 °C). For this reason the absolute accuracy of the estimated partial pressures is not very high [2]. The relative error of the partial pressures due to the reproducibility of the mass flows, pressures and temperatures was estimated to be 15% [2].

It was found [2] that the optimum parameters for pyrite (FeS_2) thin film growth are as shown in table 3. By varying the temperature it was shown that the films do not grow at a substrate temperature below 250 °C. In the range from 250 to 400 °C the growth rate obeys an Arrhenius dependence with an activation energy of 73 kJ mol^{-1} indicating a kinetically controlled growth. The growth rate from 500 to 600 °C remains approximately constant due to the mass-transport limited regime. Below 450 °C the films consist mainly of marcasite. Starting at 450 °C the fraction of pyrite increases at the expense of marcasite. Pure pyrite films were obtained above 525 °C. It was shown by RBS and atomic emission spectroscopy (AES) technique analysis that there is no significant incorporation of precursor decomposition products (C, O, CO and hydrocarbons) into the films during growth. The morphology of the thin films was studied by SEM; the cross section of the film grown at a substrate temperature of 600 °C on Si(100) reveals a columnar growth perpendicular to the Si(100) substrate with grains of up to 1.2 μm edge length.

2.2. Alumina (Al_2O_3) synthesis

Alumina thin films have found several applications both in optoelectronics and wear-resistant coatings due to their peculiar physical and mechanical properties, such as high dielectric constant, hardness, and corrosion resistance.

Dialkylaluminium acetylacetonates $Me_2Al(acac)$, $Et_2Al(acac)$ and $^{i}Bu_2Al(acac)$ were used as precursors to synthesise Al_2O_3 thin films by the low pressure MOCVD method as a result of reaction precursors with oxygen or water vapour [3].

$$(R_2Al(acac))_{gas} + O_{2\ gas}(\text{or } H_2O_{gas}) \rightarrow (Al_2O_3)_{film} + (\text{by-products})_{gas}.$$

Table 2. Metal organic compounds for FeS_2 and Al_2O_3 synthesis.

Precursors	Vapour pressure (Torr) (T, K)	$T_{synthesis}$ (°C)	Structural formula
FeS_2			
$Fe(CO)_5$	$P = 8.514–2105/T$	300–550	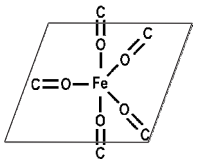
$[(CH_3)_3C]_2S_2$		300–550	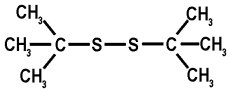
Al_2O_3			
$Me_2Al(acac)$		400–480	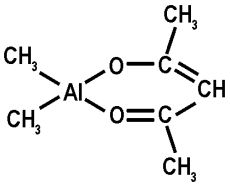
$Et_2Al(acac)$		420–520	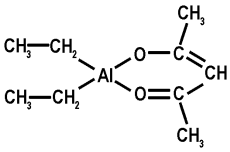
$^{i}Bu_2Al(acac)$		420–500	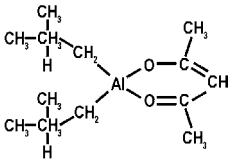
O_2; H_2O			

Structural formulae and some properties of dimethyl-, diethyl- and di-*iso*-butyl aluminium acetylacetonates are presented in table 2. All the Al_2O_3 depositions [3], on lime-glass and quartz substrates, were done in a low-pressure, hot-wall CVD reactor equipped with an in-line FTIR (Fourier transform infrared) spectrometer to monitor the exhaust gases. The reactor was a Pyrex pipe, 31 cm in length with a diameter of 4.8 cm. The temperature range investigated was 200–610 °C, and the total pressure was in range 120–400 Pa. The bath temperature was 30 °C for $Me_2Al(acac)$ and $Et_2Al(acac)$ and 70–80 °C for $^{i}Bu_2Al(acac)$.

The gas phase composition in the reaction chamber for all three precursors was studied by FTIR using a gas cell kept at 100 °C to avoid decomposition processes.

Figure 2 shows the IR transmittance spectra of the precursors in the gas phase. The vibrational wavenumbers of the principal bands, together with a proposed assignment, are reported in table 4. Precursor IR bands in the low energy region assigned to Al–O stretching lay in the region 720–690 cm^{-1}, with a slight displacement towards lower wavenumbers as the molecular complexity increased.

Deposition of Al_2O_3 thin films was achieved in the temperature range 400–480 °C for dimethyl, 420–520 °C for diethyl, and 420–500 °C for di-*iso*-butyl derivatives, using N_2

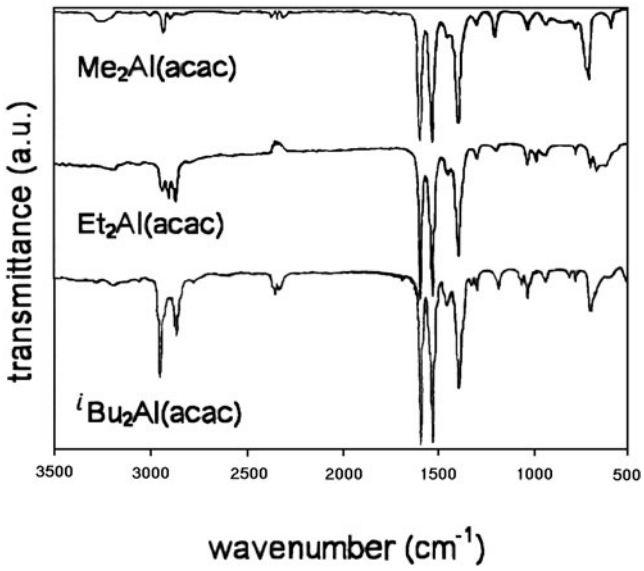

Figure 2. Gas phase IR transmittance spectra of the compounds [3].

Table 3. Standard process parameters for pyrite thin film preparation [2].

Source temperature of $Fe(CO)_5$ (°C)	−17
Source temperature of TBDS (°C)	50
Total flow (Ar) (sccm)	440
Reactor pressure (mbar)	50
Partial pressure of $Fe(CO)_5$ (mbar)	5×10^{-3}
Partial pressure of TBDS (mbar)	2
Growth temperature (°C)	575
Growth rate (Å s^{-1})	2.5

(20 sccm) as the carrier gas and O_2 (50 sccm) or water vapour (200 sccm) as the reactant gas. All the resulting films were amorphous, even after annealing at 1000 °C; α-alumina structure was detected after annealing at 1200 °C [3]. The films grown without water vapour were black and, as revealed by x-ray photoelectron spectroscopy (XPS), rich in carbon (50 at.%). Annealing of these films in air resulted in a gradual reduction of carbon content to about 5 at.%. Annealing in nitrogen did not diminish the carbon content, while annealing in oxygen alone resulted in a very slow clearing process. It is a fact, that films grown in the presence of water vapour are transparent with negligible carbon contamination. XPS of the as-grown films shows an O/Al ratio of 1.5–1.7, and a carbon concentration below the detection limit [3].

2.3. MOCVD stages and mechanisms

The whole CVD process can be divided into the following steps:

$$\begin{array}{ccccc} \text{Precursor} & & \text{Transport of gases} & & \text{Chemical reaction and} \\ \text{evaporation} & \rightarrow & \text{to substrate surface} & \rightarrow & \text{by-product exhaust} \end{array}$$

In the first step of the CVD process it is very important to know the vapour pressure dependence on temperature and vapour content. Parameters such as the melting points of the precursors, temperatures of initial mass losses, temperatures of decomposition and

Table 4. Vibrational wavenumber (cm^{-1}) [3].

Dimethyl-	Diethyl-	Di-*iso*-butyl-	Assignment
3012	2950	2958	νC–H
2938	2916	—	νC–H
2898	2877	2873	νC–H
1603	1601	1601	νC–C
1535	1535	1533	νC–O
1450	1454	1456	δCH–C=O
1396	1396	1396	δCH_3
1298	1303	1330	νC–C + νC–CH_3
1203	1207	1190	δC–H
1033	1037	1039	ρCH_3
720–707	694–668	696	νAl–O + νAl–C
588	—	—	νAl–C + νAl–O

activation energies and vapour pressure dependence on temperature come normally from thermodynamic studies of precursors (thermogravimetric (TG) analysis, differential thermal analysis (DTA), heat capacity measurements, etc). Vapour contents and precursor evaporation rates are usually studied by mass spectrometry and by FTIR spectrometry, non-intrusive and real-time techniques. It has only recently become common practice to use in-line mass and/or FTIR-spectrometers in CVD installations to monitor evaporated and exhaust gases.

The transport of gas-phase precursors to the substrate, reactor design, process control and modelling of thin film growth kinetics is a special area of research work. There are two main regimes of CVD processes—a gas flow regime (760–10^{-2} Torr) and a molecular beam regime (10^{-3}–10^{-5} Torr). The difference between these two regimes is that for the first regime two kinds of chemical reactions are realised—homogeneous reaction in the gas phase near the substrate surface and heterogeneous reactions on the surface of the substrate. For the second regime only heterogeneous chemical reactions takes place because collisions between molecules are eliminated at these vapour pressures. In the two examples of MOCVD synthesis of FeS_2 and Al_2O_3 thin films discussed above, the gas flow regime was realised. In general, growth at low temperatures ($T_g < 400\,^{\circ}C$) is kinetically limited. This means that the rate of the chemical reaction at these temperatures is not fast enough to allow all precursor molecules transported to the substrate to be transformed into a final product. At these temperatures the deposition rate increases with temperature. Assuming an Arrhenius-type dependence on the deposition temperature, the apparent activation energy of the film growth process can be estimated.

An interesting example of a pulsed MOCVD system with ultrasonic atomization of the liquid precursor was recently developed by Krumdieck and Rai [4]. Titanium dioxide (TiO_2) thin films were deposited in this work using titanium isopropoxide ($Ti(OC_3H_7)_4$) in toluene solvent as a precursor. In the experiments described [4], each pulse constitutes a two-second steady flow at the end of each 10 s pulse cycle. Thus, within each 10 s pulse cycle, the reactor conditions range from viscous to molecular flow regimes. The TiO_2 film growth rate from titanium isopropoxide was measured over the operational temperature range (400–700 °C) for each set of precursor and pulse rate conditions [4]. Growth rates were defined using two methods: *in situ* colour fringe shift rate measurements, and post-deposition thickness measurements. An Arrhenius plot of the growth rate as a function of temperature is shown in figure 3 for several different precursor concentrations, but constant pulse rate [4]. The growth rate exhibits a kinetic-controlled behaviour at temperatures below 525 °C with an activation energy of 95 ± 5 kJ mol^{-1}. The growth rate becomes limited by the precursor supply rate in the

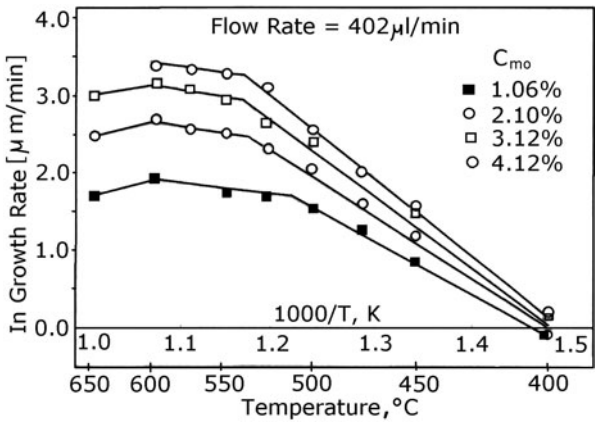

Figure 3. Arrhenius plot of experimental growth rate data for a range of precursor concentrations [4].

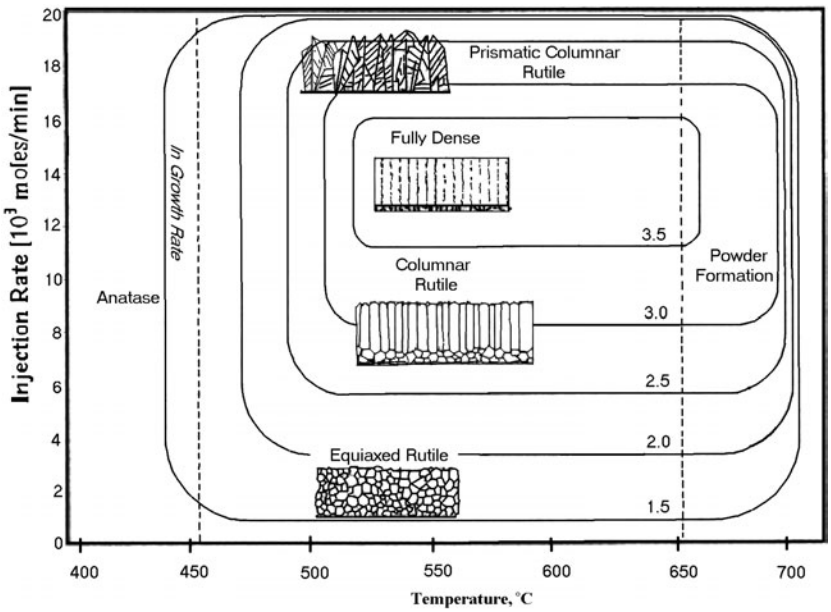

Figure 4. Microstructure and phase processing map for pulsed MOCVD of TiO_2 from $Ti(OPr^i)_4$ precursor over the range of deposition conditions [4].

temperature range 525–650 °C. At higher temperatures (>600 °C), a homogeneous vapour-phase decomposition of the precursor takes place in the vicinity of the substrate surface, and leads to the powder deposition of TiO_2 anatase phase. The microstructure of the film was studied to show the dependence on temperature and precursor injection rate [4]. The results of this study are shown in figure 4.

The detailed nature of the chemical reactions occurring in MOCVD processes have only recently begun to be elucidated. The specific reaction kinetics and thermodynamics are functions of the precursors and substrate employed, as well as the growth pressure, temperature, carrier gas and reactor geometry. As was shown above (see figure 4) hydrodynamics can also

play an important role in the final results (morphology) of growth experiments. An exact reconstruction of the chemical reactions in the gas phase and on the surface of the substrate is a very complicated problem. To reconstruct a chemical reaction it is normally necessary to use some experimental techniques, such as mass spectrometry, x-ray diffraction, tunnelling and/or atomic-force microscopy simultaneously. It is necessary to know an exact structure of the substrate surface, too. In practice all these conditions are fulfilled very rarely and only for the most simple precursor molecules and surface terminations. For example, an atomistic modelling of CVD of NO on the Si(001)(2×1) reconstructed surface [5] was recently carried out.

Some results on chemical reactions in the gas phase or on the substrate surface can be obtained with mass spectrometry [6]. Another example of such an analysis on the decomposition of $Ti(dpm)_2(OPr^i)_2$ in vacuum and in the presence of oxygen will be discussed later in this paper. The molecular beam mass spectrometry (MBMS) technique allows direct and real-time measurement of the gas phase in the reactor. It can provide quantitative concentration data on both condensable and non-condensable species, including ion, radical, and neutral species. The gases sampled undergo an adiabatic expansion, which rapidly quenches any thermal chemistry as they are formed into a collisionless beam. This allows the MBMS to take a 'snapshot' of the gas phase in the reactor. The measurement of the concentration of species present in the reactor during decomposition will elucidate the mechanism of decomposition.

3. The use of complex compounds in the CVD technique

There is a significant difference between the examples of CVD applications for pyrite (FeS_2) and alumina synthesis and synthesis of TiO_2 thin films discussed above. In the first two examples, in order to synthesize the two-component compound it was necessary to use two precursors:

$$\text{Precursor (A)} + \text{Precursor (B)} \rightarrow \text{AB}.$$

In the case of TiO_2 synthesis, the precursor (titanium isopropoxide ($Ti(OC_3H_7)_4$)) contains components of which, the resulting compound is formed:

$$\text{Precursor (A–B)} \rightarrow \text{AB}.$$

It was not necessary to supply the CVD chamber with additional oxygen to prepare the TiO_2 thin film. This means that the Ti–O bonds are strong enough and some of them were not being destroyed in the precursor decomposition process during thin film growth. The kinetics of thin film growth is different for such a mechanism than can be expected for two-component reactions.

Therefore, the main feature of complex compound usage is that every molecule of the complex compound (CC) contains a 'ready-made' fragment of the desired structure. For all the examples discussed below, the growth of the thin film takes place in vacuum (molecular beam regime) on the surface of the substrate. As will be shown, the existence of ready-made bonds in the CC is very productive for material preparation by the CVD method. In the following some materials and corresponding CC precursors are presented.

3.1. Electroluminescent ZnS:Mn films

A promising approach in the synthesis of ZnS films is the use of complex compounds of zinc(II) with sulfur-containing ligands from the dithiocarbamate ($Zn(S_2CNR_2)_2$) and

Table 5. Examples of complex compounds and their structural formulas.

ZnS	$ZnPhen(Et_2NCS_2)_2$	[7, 8]	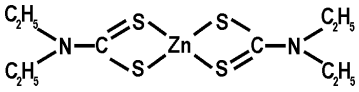
	$Zn(2,2'\text{-bipy})(i\text{-}PrOCS_2)_2$	[7, 9]	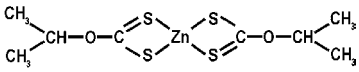
ZnS:Mn	$ZnPhen(Et_2NCS_2)_2$ + $MnPhen(Et_2NCS_2)_2$	[10]	
ZnS:Mn	$Zn(2,2'\text{-bipy})(i\text{-}PrOCS_2)_2$ + $Mn(2,2'\text{-bipy})(i\text{-}PrOCS_2)_2$	[11]	
EuS	$EuPhen(Et_2NCS_2)_3$	[12]	
ZnS:Eu EuS:Zn	$ZnPhen(Et_2NCS_2)_2$ + $EuPhen(Et_2NCS_2)_3$	[12]	
ZnS:Tb	+ $TbPhen(Et_2NCS_2)_3$	(Unpublished)	
ZnS:Sm	+ $SmPhen(Et_2NCS_2)_3$	(At press)	
Sm_2S_3			
In_2S_3	$In(S_2COC_3H_7\text{-iso})_3$	[13, 14]	
In_2O_3 : S			
TiO_2	$Ti(dpm)_2(OPr^i)_2$	[15, 16]	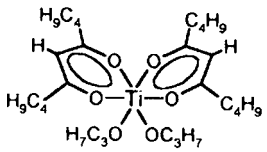
FeS_2 (pyrite)	$FePhen(Et_2NCS_2)_3$	[28]	

xanthate ($Zn(S_2COR)_2$) classes (table 5). The mixed-ligand CCs ZnL_2 and MnL_2 with 1,10-phenanthroline (Phen) with the compositions $ZnPhenL_2$ (compound 1) and $MnPhenL_2$ (compound 2) were synthesized. The choice of these CCs was justified for a number of reasons. Firstly, Mn^{2+} preserves the oxidation state 2+ by the presence of the L ion in the mixed-ligand CC, otherwise the oxidation process $Mn^{2+} \rightarrow Mn^{3+}$ takes place. Secondly, compounds 1 and 2 sublimate on heating in vacuum. Thermal analysis of CCs 1 and 2 in vacuum (approximately 0.1 Pa) was carried out using a Setaram derivatograph at a heating rate of 5° min^{-1} with a 10 mg sample. The weight loss temperature range for compound 1 was 90–230 °C at 100% loss of mass. For compound 2, the weight loss temperature range was 160–260 °C at 98% loss of mass, which indicates the volatility of these compounds. These results imply that the temperature range best suited for co-vapourization of these CCs is 160–230 °C. The use of ZnL_2 with its weight loss temperature range of 90–180 °C narrows the region of overlap of the sublimation temperatures for ZnL_2 and compound 2. Furthermore, ZnL_2 melts at 178 °C and complex 1 at a higher temperature (260 °C). These CCs are sufficiently stable under atmospheric conditions, non-hygroscopic, flame-proof and non-explosive.

As starting compounds of the xanthate class, newly synthesized mixed-ligand CCs were used: zinc(II) and manganese(II) isopropylxanthates with 2,2′-bipyridyl (bipy) ($Zn(2,2'\text{-bipy})(S_2COC_3H_7\text{-}i)_2$ (compound 3) and $Mn(2,2'\text{-bipy})(S_2COC_3H_7\text{-}i)_2$ (compound 4)). The weight loss temperature ranges for compounds 3 and 4 were 70–130 °C (100% weight loss) and 110–172 °C (87.5% weight loss) respectively. The temperature range most suitable for

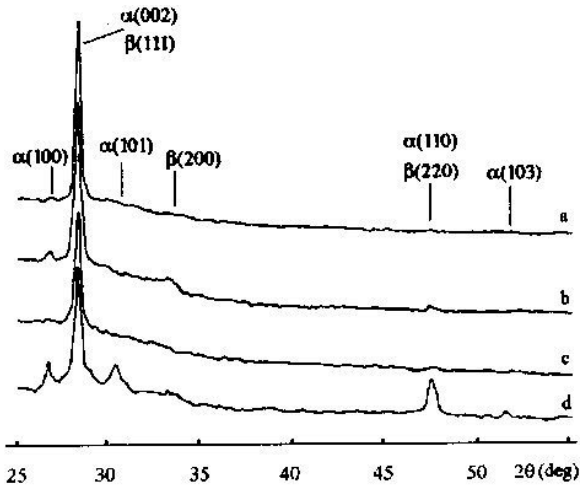

Figure 5. X-ray diffraction spectra of ZnS:Mn films synthesized from compounds 1 and 2 at $C_{Mn} = 0.1$, 0.3 and 0.6 wt% for curves a, b and c (samples 38, 37 and 36) respectively. Curve d refers to a ZnS film synthesized from compound 3 (sample 32).

co-evaporation is 110–130 °C. In common with the mixed-ligand dithiocarbamates 1 and 2, compounds 3 and 4 are sufficiently stable under atmospheric conditions, flame-proof, non-explosive and non-hygroscopic.

The ZnS and ZnS:Mn films were prepared in a standard vacuum apparatus with an oil diffusion pump and a liquid-nitrogen trap producing a maximum vacuum of 8×10^{-7} Torr (the pressure of the decomposition products during deposition was 10^{-3}–10^{-4} Torr). The fabrication conditions of ZnS:Mn thin films are shown in table 6. The temperature of the evaporator was regulated between 20 and 400 °C.

According to qualitative x-ray phase analysis, polycrystalline films were obtained: cubic (β) and/or hexagonal (α) modifications of the corresponding sulfides [17]. The identification of the mixture of these phases was complicated by considerable overlap of the diffraction reflections (see figure 5). In our case, the situation was aggravated by the texture of the films (along [100] for the α and [111] for the β modifications), which rendered a number of reflections weak or virtually absent and precluded quantitative analysis.

Thus when compound 1 was used as the starting compound, β-ZnS films were obtained, whereas the use of a mixture of compounds 1 and 2 (Mn doping) produced a mixture of α and β phases. When compound 3 was taken as the precursor or when the films were doped with Mn (mixture of compounds 3 and 4), the α modification was obtained, whose unit cell parameters were changed in comparison with pure α-ZnS [17].

The EPR spectra obtained are shown in figure 6. In curve a (film grown from dithiocarbamate complexes), there is a sextet of narrow lines of superfine structure (STS) with $g = 2.00$ and $A = 6.9 \times 10^{-3}$ T, which implies the presence of single non-interacting Mn^{2+} ions. The increase in the Mn content in the charge results in a gradual broadening of the spectral lines (curve b). At the 2:100 concentration, the EPR spectrum takes the form of a broad line (curve d). In the case of a non-uniform distribution of Mn^{2+} ions, the EPR spectrum is a superimposition of the SFS sextet and a broad line with the same g factor and a half-width $\Delta H = 1.25 \times 10^{-2}$ T (curve c). An analysis of the broad line by the linear anamorphosis method showed that it is described by a Lorentzian function. Its appearance is probably due to regions of the film with high local concentrations of Mn^{2+} ions, which leads

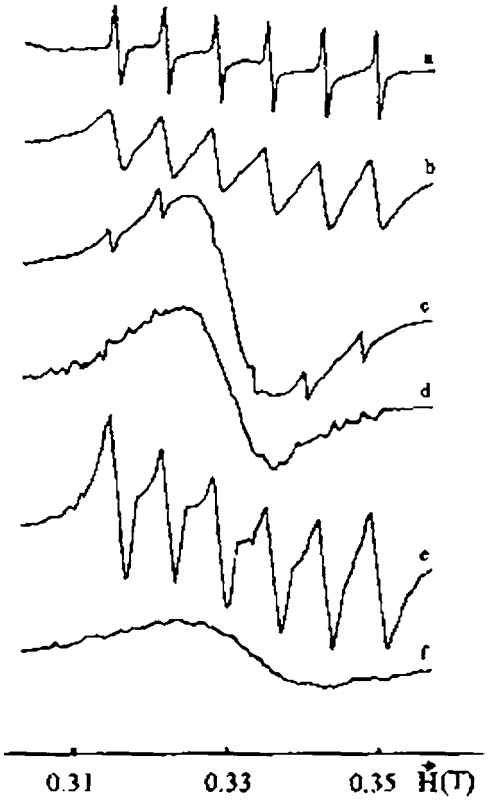

Figure 6. EPR spectra of ZnS:Mn films. Curves a, b, c and d: films synthesized from compounds 1 and 2 with concentrations $C_{Mn} = 0.1, 0.6, 1.0$ and 2.0 wt% (samples 38, 36, 35 and 39) respectively. Curves e and f: samples 56 and 66 synthesized from compounds 3 and 4 with $C_{Mn} = 1$ and 10 wt%.

to strong exchange interaction averaging and narrowing of the SFS from Mn^{2+}. As a rule, such films are characterized by a relatively weak EL that does not correspond to the change in manganese concentration.

It has been shown that, by using mixed-ligand CCs of diethyldithiocarbamates and isopropyl-xanthates of zinc(II) and manganese(II) with 1,10-phenanthroline and 2,2′-bipyridyl, it is possible to prepare electroluminescent ZnS:Mn films at temperatures of 220–450 °C by the CVD method. It has been found by the EPR method that Mn^{2+} ions enter the ZnS crystal lattice as single centres and are uniformly distributed over the film. In the samples obtained from xanthate complexes, the region of observation of the SFS sextet extends to higher Mn concentrations. It is advantageous that the luminophore films require no additional annealing after preparation to make the distribution of the dopant uniform. The properties of the luminophore films obtained allow the recommendation of this new technique for the fabrication of electroluminescent displays.

3.2. Synthesis and properties of ZnS–EuS thin films

The preparation of $A^{II}B^{VI}$ films doped with rare earth (RE) elements attracts significant attention due to their potential application in microelectronics. The incorporation of RE

elements into the $A^{II}B^{VI}$ lattice and the mechanisms of isovalent and heterovalent replacement have been discussed in the literature since 1960. It has been shown for single crystalline materials synthesized at temperatures above 1000 °C that the solubility of RE elements in ZnS is relatively small and lies in the interval of 10^{-4}–10^{-2} at.% [18, 19]. Therefore, preparing homogeneous solid solutions for these systems presents significant difficulties, and doping, as a rule, results in dopant segregation and clustering enhanced by extended structural defects or crystallite boundaries.

We have used complex compounds of the class of dithiocarbamate, $ZnPhen(S_2CNEt_2)_2$ (hereafter referred to as compound 1) and $EuPhen(S_2CNEt_2)_3$ (compound 2) to prepare ZnS–EuS films. These CC are sufficiently stable under ambient conditions, non-hygroscopic, and of low toxicity. The choice of compounds 1 and 2 for film synthesis is based on the fact that these compounds easily sublimate at relatively low temperatures. The temperature conditions for compound sublimation have been determined using differential thermal analysis/thermal gravimetry (DTA/TG).

Quasi-equilibrium TG (Derivatograph Q-1500-D, MOM Company, Hungary) has been used in the regime of constant mass loss rate (0.3 mg min^{-1}) to determine the temperature conditions and character of evaporation. At a vapour pressure of about 6.8 Torr, compounds 1 and 2 sublimate without decomposition at temperatures 253 and 223 °C, respectively. The optimal temperature range 220–260 °C for co-evaporation of the CC of Zn and Eu has been established as a result of this study.

A special evaporator has been designed for simultaneous evaporation of Zn and Eu compounds from an open surface. It is possible to control the ratio of the components and to provide necessary molecular flow densities during the process to sustain high and stable growth rates of the films. At temperatures used in the evaporator (200–260 °C), the total pressure in the chamber varies in the range 10^{-5}–10^{-4} Torr. This allows work in the regime of a molecular vapour stream.

Glass, fused quartz and silicon wafers ((111) orientation) have been used as substrates (substrate areas from 0.5 to 54 cm^2). All substrates were cleaned carefully by a special procedure immediately before loading. This procedure is described as follows: the glass and fused quartz are washed in a detergent solution, rinsed in distilled water, and immersed in H_2SO_4:$K_2Cr_2O_7$:H_2O (184:6:100 by mass) for 24 h. Then the substrates are thoroughly washed in distilled water and dried in a flow of boiling propan-2-ol. The silicon substrates are treated by a polished technique [8]. The thickness of the residual oxide layer on silicon, according to ellipsometry, is 9–13 Å. During one deposition experiment, different substrates can be used by placing them in the isothermal zone.

Film characterization included x-ray diffractometry (XRD), Raman spectroscopy, chemical phase analysis, ellipsometry, and spectrophotometry. The XRD of the samples was carried out using a DRON-UM 1 diffractometer ($R = 192$ mm, Cu Kα radiation, Ni filter, and scintillation detector with amplitude discrimination) in the range of 2θ angles from 5° to 70° at room temperature. Raman spectroscopy was performed using a spectrometer triplemate (SPEX) with multichannel registration (detector O-SMA, SI) in backscattering geometry. The 488 nm Ar^+ laser line was used for excitation.

For chemical composition analysis of the films, a new method of differential dissolution has been used [20]. The procedure includes dissolution of the film in a reactor of the apparatus described in [20]. The films are dissolved in the flow of an HNO_3 solvent with concentrations increasing from 0.01 to 0.1 M. The amounts of Zn, S, and Eu passed to the solution are determined every 15 s using AES with an inductively connected Ar plasma reactor (uncertainty about 3–5%). Routinely about 150–200 points obtained have been used to reconstruct the kinetic curves of dissolution for these elements and their stoichiogram (molar ratio Zn/S,

Table 6. Fabrication conditions for ZnS:Mn films.

Sample number	Initial mixtures	C_{Mn} (wt%)	T_{synth} (°C)	d (nm)
38	$ZnPhenL_2 + MnPhenL_2$	0.1	450	340
37	$ZnPhenL_2 + MnPhenL_2$	0.3	450	310
36	$ZnPhenL_2 + MnPhenL_2$	0.6	450	340
35	$ZnPhenL_2 + MnPhenL_2$	1.0	450	300
39	$ZnPhenL_2 + MnPhenL_2$	2.0	450	220
32	$Znbipy(S_2COC_3H_7\text{-}i)_2$	—	300	520
56	$Znbipy(S_2COC_3H_7\text{-}i)_2 + Mnbipy(S_2COC_3H_7\text{-}i)_2$	1.0	220	260
66	$Znbipy(S_2COC_3H_7\text{-}i)_2 + Mnbipy(S_2COC_3H_7\text{-}i)_2$	10.0	220	330

Eu/S, and Eu/Zn). This method allows the chemical composition to be determined as a function of film depth for each phase in the film.

The refractive indices and film thicknesses have been determined using ellipsometry (ellipsometer LEF-3M, $\lambda = 632$ nm) and spectroscopy in the region of visible light (spectrophotometer SF-18). First, the film thickness was estimated from the reflection spectrum. Then the inverse problem of ellipsometry was solved using the one-, two-, and three-layer films model [21].

As has been shown previously, ZnS films from $ZnPhen(S_2CNEt_2)_2$ can be prepared at $T = 400$–$450\,^{\circ}C$ [7]. In the present work, films of cubic ZnS were deposited on different substrates at $T = 450$–$530\,^{\circ}C$. The crystal structure improves when the substrate temperature increases. This follows from the increase of the reflection intensities and the reduction of the half-widths of the reflections on the diffractograms. When only compound 2 is used as a precursor, EuS films are formed at substrate temperatures 490–530 °C. Simultaneous evaporation of Zn and Eu compounds leads to the deposition of ZnS:Eu films for substrate temperatures 490–530 °C. The lowest substrate temperature is limited by the temperature of decomposition of both Zn and Eu CCs resulting in the formation of the sulfides.

The highest value of the substrate temperature is restricted by the interactions of the sulfides with the substrate materials and by the contamination of the films by products of decomposition of the CC. The interaction effect has been established by the detection of contamination of the films by Si from the substrates using chemical analysis. The interaction of the sulfides with the glass substrates begins at $T = 520\,^{\circ}C$. For quartz and silicon, such interaction has not been observed up to 530 °C. However, starting at 530 °C, black inclusions of carbon have been observed in the films. The deposition conditions (temperatures of evaporator and substrates, molar ratio of Zn and Eu compounds, thermal treatments) have been varied. Some parameters of the process and composition of the films are presented in table 7.

It can be seen from table 7 that, as a whole, an increase in the Eu CC fraction in the evaporator leads to an increase in the Eu concentration in the film. The difference observed between these two concentrations may be explained by an incomplete sublimation for both volatile compounds, as well as by an insufficient accuracy of Eu determination, when Eu in the analysed solution is in the range 10^{-7}–10^{-6} mol ml^{-1}. The deposition rate depends on a number of parameters, including, first of all, the temperatures of the substrate and evaporator and the vapour pressure. At optimal conditions, a deposition rate of 20 nm min^{-1} can be achieved. The film thickness is uniform over the substrate area 6×9 cm^2. The thickness of the films on silicon substrates is systematically higher than on glass substrates. As a result of this study, the conditions for reproducible deposition of ZnS:Eu films with a controllable doping level have been found.

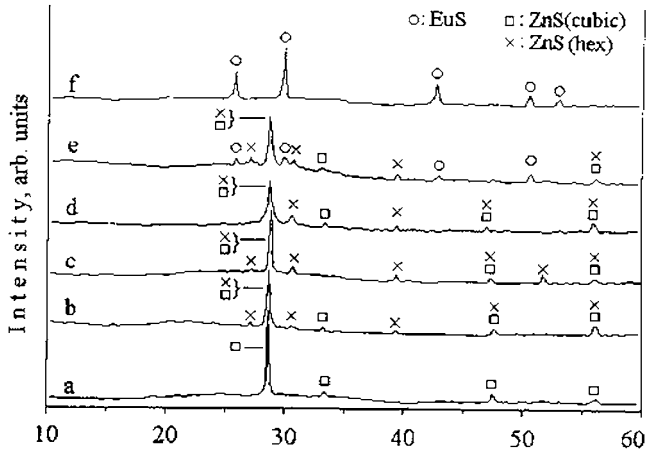

Figure 7. X-ray diffraction spectra of ZnS, EuS, and ZnS:Eu films synthesized from compound 1 (curve a, sample 2), compound 2 (curve f, sample 14), and compounds 1 and 2 (curves b–e, samples 7, 8, 11, and 13, respectively).

Table 7. Characteristics of ZnS–EuS Films.

		Eu concentration $C_{Eu}/(C_{Zn} + C_{Eu})$		
Sample	T_{dep} (°C)	In evaporator (at.%)	In film (at.%)	Film thickness (nm)
1	490	0	0	535
2	520	0	0	700
3	490	0.09	0.003	577
4	490	0.21	0.12	577
5	490	0.4	0.2	530
6	530	0.66	0.42	235
7	510	0.74	0.6	540
8	500	0.83	1.1	1365
9	510	0.9	0.41	416
10	530	1.5	1.3	480
11	515	1.7	1.4	220
12	510	3.9	1.9	810
13	530	6.9	4.8	280
14	530	100	100	220
15	490	100	100	560

The structures of the films have been studied by XRD and Raman spectroscopy. Figure 7 shows the x-ray diffractograms of ZnS (curve a), EuS (curve f), and ZnS:Eu (curves b, c, d, and e) films on quartz or glass substrate.

According to XRD phase analysis, the reflections for the polycrystalline films correspond to cubic (β) and/or hexagonal (α) modifications of ZnS, and cubic modification of EuS. The exact identification of the ZnS phases is complicated by a considerable overlap of the diffraction reflections belonging to α-ZnS and β-ZnS. Identification of the hexagonal modification follows from the observed closest stereographic projections of reflections (102) and (101) with angular positions 39.64° and 30.56°, respectively. The presence of the cubic modification has been

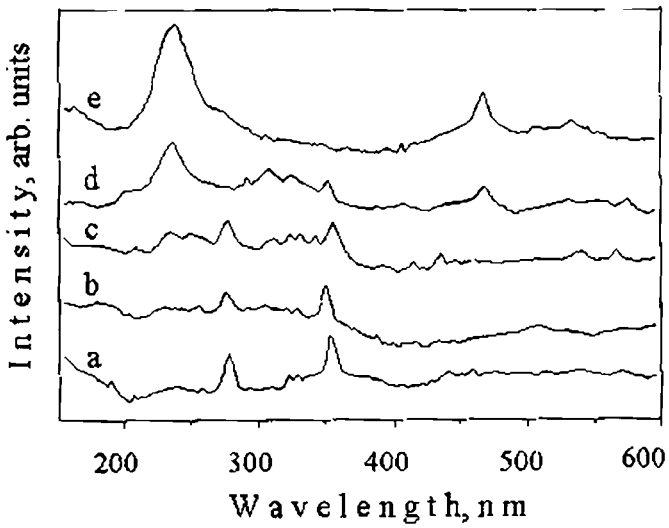

Figure 8. Raman spectra of ZnS, EuS, and ZnS:Eu films, synthesized from compound 1 (curve a, sample 2). Compound 2 (curve e, sample 14), and compounds 1 and 2 (curves b, c, and d, samples 7, 8, and 13, respectively).

checked using the (200) reflections at 33.14°. In this case, the closest directions overlap with the reflections of the hexagonal modification. The EuS films do not have a preferable orientation; all reflections on the diffractograms are well-defined, and the ratio of the intensities is close to the values presented in table 7.

The effects of Eu doping start to appear at very low concentrations of Eu in ZnS. The cubic ZnS reflections become broader and the reflections of hexagonal ZnS appear. At Eu concentrations of more than 2 at.% (curve e), the reflections observed on the diffractogram can be attributed to the ZnS and EuS phases; the structural non-homogeneity of the films increases. It appears that the incorporation of Eu results in disorder of the cubic ZnS structure and may cause defect formation in the layers.

Raman spectra of films on glass or silicon are shown in figure 8. It can be seen that all the main features for crystalline ZnS and EuS are present: first-order modes at 275 cm^{-1} (TO phonon), at 350 cm^{-1} (LO phonon) for ZnS (curve a), and at 240 cm^{-1} for EuS (curve e), as well as lines of second order for ZnS, and the double frequency at 480 cm^{-1} for EuS [22–24]. In the spectra of ZnS:Eu films (curves b, c and d), the intensities of lines related to the ZnS phase decrease rapidly, and at Eu concentration in the films of about 5 at.% (curve d), together with weak modes of ZnS, the EuS modes have been observed.

One explanation for such variation is that the ZnS lattice is significantly affected by the presence of Eu atoms. The defect's formation violates the selection rules for the perfect ZnS lattice, and the shape and intensity of the observed Raman scattering reflects the density of phonon states of the crystal structure with defects, rather than the process of scattering in the centre of Brillouin zone of a perfect lattice.

Kinetic curves of differential dissolution of each element Zn, Eu, and S, for pure ZnS (a), EuS (b), and ZnS:Eu (c) samples are presented in figure 9. Also shown are the stoichiograms Zn/Eu in the (c) case (the similarity of Zn and S or Eu and S kinetic curves is obvious). From curves a and b, we conclude that pure ZnS and EuS are highly stoichiometric, independent of the film thickness. In the case of curve c, the figure shows the dissolution of a tricomponent

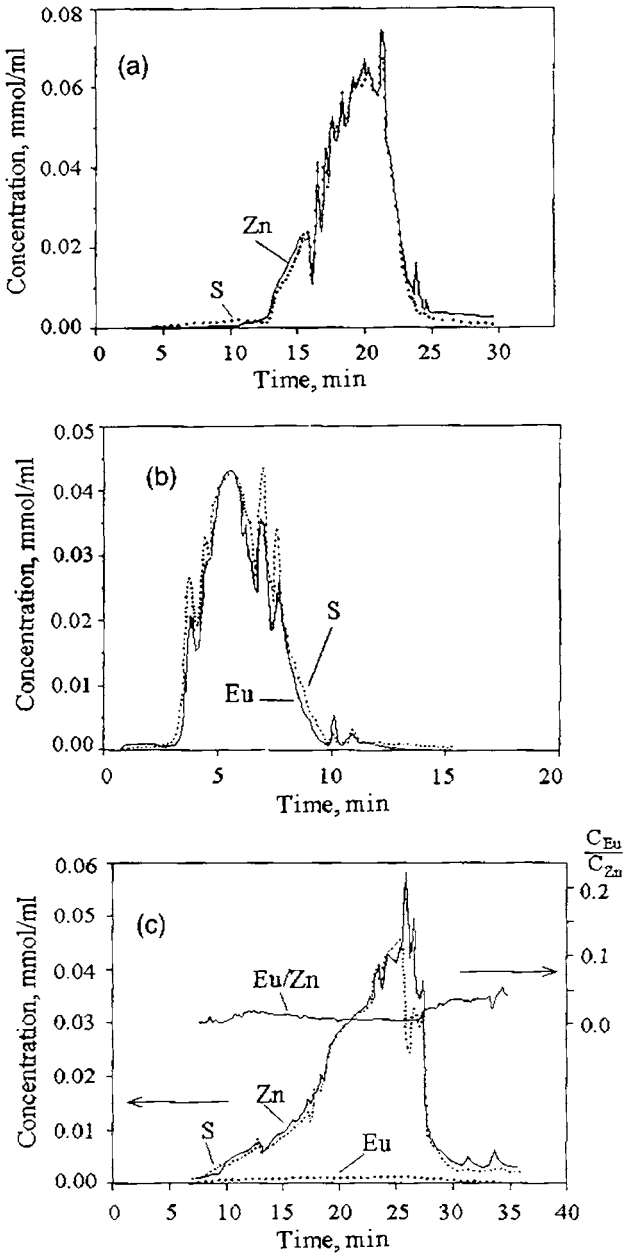

Figure 9. Kinetic curves of solution for ZnS films (sample 2) (a), for EuS (sample 14) (b), and kinetic curves of solution and stoichiogram for ZnS:Eu film (sample 7) (c).

sulfide with Eu/Zn ratio 0.006 ± 0.002. The sulfide is considered to be a solid solution ZnS:Eu, since the XRD patterns of the film show no indications of second phases.

It has been shown that the volatile complex compounds $ZnPhen(S_2CNEt_2)_2$ and $EuPhen(S_2CNEt_2)_3$, can be successfully used as precursors for CVD deposition of ZnS and EuS films in the temperature range 490–530 °C. ZnS films doped by Eu have been obtained using

simultaneous evaporation of Zn and Eu CC. The properties of ZnS films are very sensitive to doping, as has been shown in this study, by a variety of methods. Conditions for the formation of a homogeneous solid solution of ZnS:Eu with concentration up to 0.3 at.% have been found. This concentration is observed to be uniform for the whole thickness of the film and is higher than that known for single crystals, about 0.02 at.% [19]. Two factors may be responsible for this increase of Eu solubility:

(i) the higher disorder (relative to that of a single crystal) of the films prepared at moderate temperatures, and
(ii) stable transport conditions for the constituent elements provided by the CVD process.

At these deposition conditions, the solubility of Eu in ZnS films reaches 0.3 at.%, which is much higher than the value for ZnS single crystals.

3.3. TiO_2 thin film synthesis

Photocatalytic TiO_2 films on glass and quartz plates were obtained by CVD using $Ti(dpm)_2(OPr^i)_2$ (dpm = 2,2,6,6-tetramethylheptane-3,5-dione, Pr^i = isopropyl) complex compound (see table 5).

It is generally believed that the presence of a ready-made fragment of the material to be deposited (such us O–Ti–O) in the source molecule accelerates the kinetics of thin film growth, and effectively permits the reduction of the synthesis temperature. In addition, the O–Ti–O groups promote oxide phase formation independently of O_2 presence in the gas phase.

The thermal behaviour of the compound in the solid state was studied by TG/DTA *in vacuo* 20 Pa (Sinku-Riku TA7000, sample 10 mg) and in Ar flow (Sinku-Riku TA7000/TGD7000RH, sample 22 mg).

Data on the thermal stability of the compound vapour and decomposition products under molecular flow conditions were obtained by a variant of a method of high-temperature mass spectrometry (figure 10). Thermolysis of $Ti(dpm)_2(OPr^i)_2$ vapours was investigated at 130–500 °C *in vacuo* and in the presence of O_2. The temperature of the evaporator varied within the range 125–150 °C. The characteristic feature of its mass spectrum is the absence of a molecular ion peak. But the absence of peaks with m/z exceeding 532 (molecular weight of the compound) indicates the monomer composition of the gas phase.

The films of TiO_2 were obtained in a standard vacuum apparatus with a turbo-molecular pump (ALCATEL TMP 5400 CP) producing a maximum vacuum of $\sim 5 \times 10^{-7}$ mbar. Vapourization was conducted from an evaporator with an open surface. The temperature of the vapour source was varied in the range 90–210 °C and the substrate temperature was stabilized in the range 450–600 °C. In the process of film deposition the pressure of volatile products of decomposition of the starting compound was $1.2–2.0 \times 10^{-4}$ mbar depending on the parameters of the process. At this vacuum it was possible to work in the regime of a molecular vapour stream. The size of the vacuum chamber allowed the vapour–substrate distance to be varied from several centimetres to 40 cm.

Glass or fused quartz plates of 7 cm × 10 cm were used as substrates. All substrates were cleaned carefully by a special procedure immediately before loading. The film thickness was determined by weight and usually was 100–300 nm. The growth rate could be varied from several nanometres to several tens of nanometres per minute.

Much attention was paid to the study of $Ti(dpm)_2(OPr^i)_2$ vapour conversions on the heated surface. It should be emphasized that the data obtained refer to the thermal decomposition of the compound vapour on the surface. To a great extent this corresponds to the actual process of CVD.

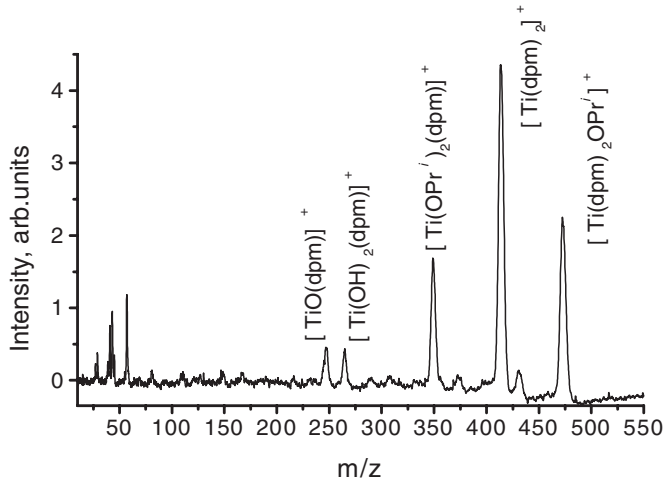

Figure 10. Mass spectrum of $Ti(dpm)_2(OPr^i)_2$ (70 eV, 150 °C).

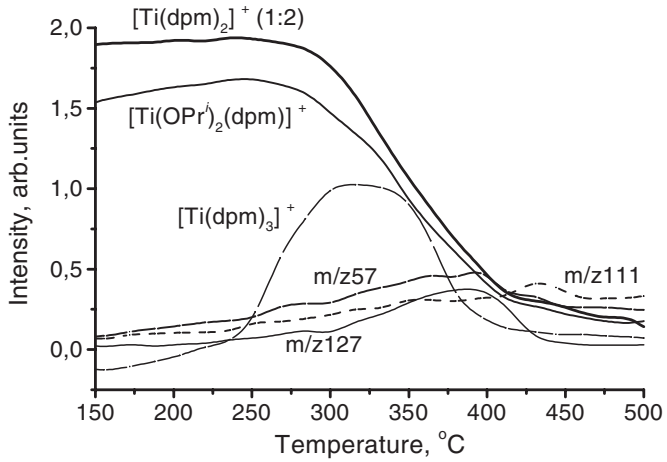

Figure 11. Temperature dependences of the ion peak intensity in mass spectra upon thermal decomposition of $Ti(dpm)_2(OPr^i)_2$ *in vacuo*.

The main feature of the compound thermolysis is the appearance of an ion with m/z 597 in the mass spectrum at a temperature >210 °C. This indicates that thermal decomposition of $Ti(dpm)_2(OPr^i)_2$ vapours begins at this temperature (see figure 11). We believe that this peak corresponds to a complex of titanium (III) with dipivaloylmethane—$Ti(dpm)_3$—resulting from the reaction between molecules of the initial compound on the heated surface. The greatest amount of decomposition is observed at a temperature >430 °C. Among the decomposition products are Hdpm (represented by the intensive peak with $m/z = 127$), organic products with m/z 111, 109, 81, different hydrocarbons with m/z 57 and 41, 43 and other light products (H_2O, CO).

From the data above, the following scheme of thermal conversions of $Ti(dpm)_2(OPr^i)_2$ on the hot surface is proposed *in vacuo*:

$$\begin{array}{c} \mathrm{Ti(dpm)_{3(gas)}} \\ \downarrow\uparrow \\ \mathbf{2Ti(dpm)_2(OPr^{\mathit{i}})_{2(ads)}} \rightarrow \mathrm{Ti(dpm)_{3(ads)} + TiO_{2(solid)} + organics\uparrow} \qquad \text{(I)} \\ \downarrow \\ \mathrm{TiO_{2(solid)} + organics\uparrow.} \qquad \text{(II)} \end{array}$$

Thermal decomposition in the presence of oxygen begins at 270 °C. The $[Ti(dpm)_3]^+$ particle is absent in mass spectra within the same temperature interval upon vapour decomposition in the presence of oxygen, indicating the difference in decomposition reaction mechanism on the surface in this case and *in vacuo*. It is clear that oxygen prevents the reduction of Ti(IV) to Ti(III). Only ions with m/z lower 57 are registered in the mass spectra at 500 °C representing such products as hydrocarbons, H_2O, CO, CO_2. This testifies to the complete decomposition of the initial compound at this temperature.

Thus we propose that the decomposition of $Ti(dpm)_2(OPr^{\mathit{i}})_2$ on a hot surface in the presence of oxygen proceeds in one stage:

$$\mathbf{Ti(dpm)_2(OPr^{\mathit{i}})_{2(ads)}} \rightarrow \mathrm{TiO_{2(solid)} + organics\uparrow.}$$

At the same time we noted the appearance and fast growth of a peak with m/z 373 in mass spectra at rapid cooling of the reactor from 500 to 350 °C. This peak corresponds to $TiO(dpm)_2$. A simultaneous rise in the peak intensity for organic products was also observed. This demonstrates the possibility of another route of vapour decomposition in the presence of at oxygen on the heated surface:

$$\begin{array}{c} \mathrm{TiO(dpm)_{2(gas)}} \\ \downarrow\uparrow \\ \mathbf{Ti(dpm)_2(OPr^{\mathit{i}})_{2(ads)}} \rightarrow \mathrm{TiO(dpm)_{2(ads)} + organics\uparrow} \\ \downarrow \\ \mathrm{TiO_{2(solid)} + organics\uparrow.} \end{array}$$

It should be noted that this route is not the main one, and it occurs at non-equilibrium conditions only, e.g. in the case of rapid heating of the reactor.

Thus the results obtained confirmed $Ti(dpm)_2(OPr^{\mathit{i}})_2$ to be decomposed producing TiO_2 independent of the presence of oxygen.

The structural phases that can be formed in a titanium dioxide sample are the amorphous phase, the metastable crystalline forms, brookite and anatase, and the high-temperature stable phase rutile [25]. The three metastable forms all occur in nature, although rutile is much the most common. It should be noted that other oxides, Ti_2O, TiO, Ti_2O_3, Ti_3O_5 and Ti_nO_{2n-1} ($n = 4, \ldots, 10$) may be formed at low oxygen concentrations.

The transition from the amorphous to the anatase form usually requires temperatures close to 300 °C. The phase transition anatase → rutile occurs in the range 600–800 °C upon heating of a TiO_2 powder sample [25]; the back transition does not occur upon cooling because of the high activation energy. In the case of bulk samples, the anatase-to-rutile phase transition occurs at temperatures over 800 °C.

Although previous CVD deposition runs on ordinary glass substrates at 520–550 °C have produced polycrystalline anatase modifications as verified by x-ray qualitative analysis [15], further attempts to reproduce this polycrystalline form on other substrates, that would be stable at the deposition temperature, did not succeed well.

Single-phase rutile (R) films were obtained after CVD deposition at temperatures close to 500 °C on Si wafer substrates. Post-synthesis annealing does not modify the structure of the as-deposited films since rutile is the stable high-temperature phase.

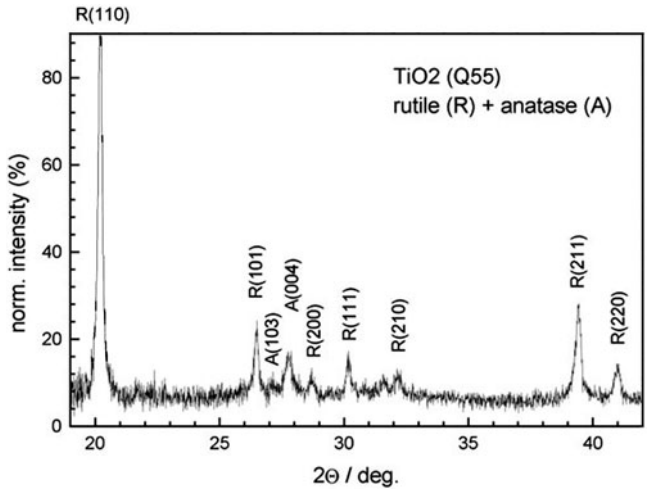

Figure 12. GIXRD pattern of as-deposited TiO_2 film on quartz. Both rutile (R, dominant phase) and anatase (A) phases are present. Deposition temperature 450 °C, film thickness ≈300 nm.

For samples deposited on fused quartz substrates, a representative grazing incidence x-ray diffraction pattern is shown in figure 12. Along with Bragg reflections corresponding to the major (R) rutile phase, several low-intensity anatase diffraction peaks could also be detected. Further annealing of these TiO_2 films in order to increase the oxygen thin film content leads to the disappearance of the minor anatase phase, so that single-phase rutile films are obtained.

3.4. Iron sulfide thin film synthesis

Iron sulfide thin films on glass, quartz, silicon (100) and mica plates were obtained by CVD using tris(diethyldithiocarbamato)iron(III) $Fe[(C_2H_5)_2NCS_2]_3$ (see table 5).

Iron sulfide films were obtained in a standard vacuum apparatus with a turbo-molecular pump (ALCATEL TMP 5400 CP) producing a maximum vacuum of $\sim 5 \times 10^{-7}$ mbar. Vapourization was conducted from an evaporator with an open surface. The temperature of the vapour source was varied in the range 180–270 °C and the substrate temperature was stabilized in the range 340–550 °C. In the process of film deposition the pressure of volatile products of decomposition of the starting compound was 10^{-4}–2.0×10^{-3} mbar depending on the parameters of the process.

The mass of the precursor used for deposition was in the range 0.065–2.000 g; this resulted in a thin film thickness in the range 30–1100 nm. The growth velocity was between 7 and 62 nm min^{-1}. When the temperature of the substrate was $\leqslant$ 320 °C no film was registered on the substrate.

The crystal structure of the iron sulfide thin films was studied by the grazing incidence x-ray diffraction method at DESY Hamburg synchrotron laboratory (HASYLAB) (see figure 13).

For samples deposited on fused quartz substrates at 340 °C the crystal structure can be attributed to Fe_9S_{10} (JCPDS-ICDD 34-1470) [17]. There are a lot of crystal modifications for the Fe–S system depending on the sulfur content but for our process the main features of Fe_9S_{10} are present for all thin films.

It is possible to compare two processes of iron sulfide thin film growth. The first process [2] is described above, uses the MOCVD technique and is based on the employment of two precursors—$Fe(CO)_5$ and TBDS. The second one is based on complex compound $Fe[(C_2H_5)_2NCS_2]_3$ usage. It is supposed that 'ready-made' fragments of Fe–S

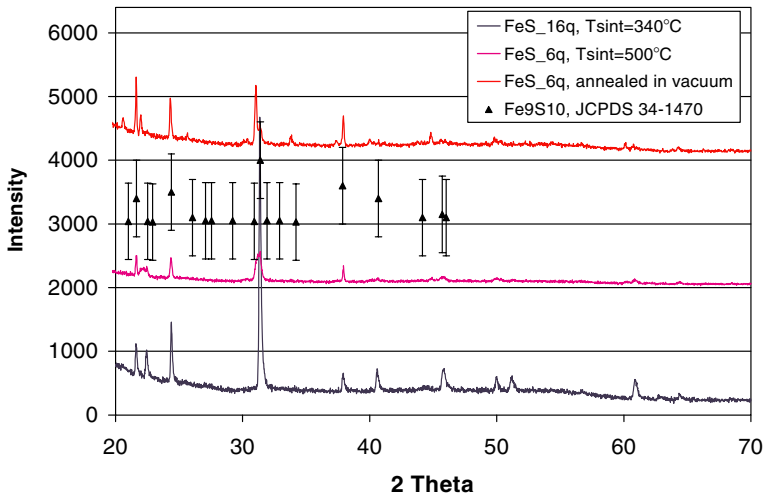

Figure 13. GIXRD pattern of as-deposited and annealed in vacuum iron sulfide thin films on quartz substrates.

(This figure is in colour only in the electronic version)

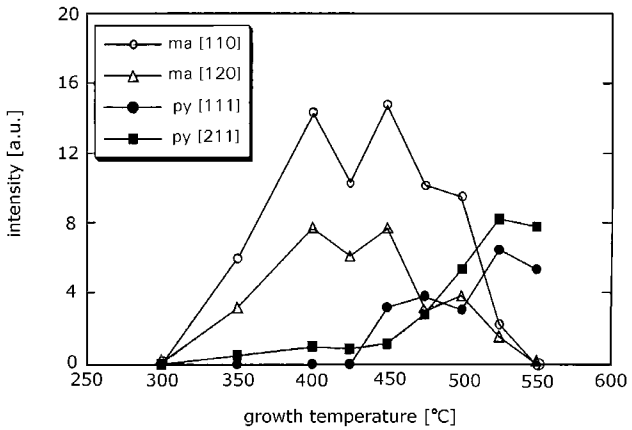

Figure 14. Integral intensities of the marcasite [110] and [120] as well as the pyrite [111] and [211] peaks of the x-ray diffraction pattern [2].

in $Fe[(C_2H_5)_2NCS_2]_3$ molecules will promote the pyrite modification of the crystal structure. There are six atoms of sulfur for one atom of iron in the $Fe[(C_2H_5)_2NCS_2]_3$ precursor molecule, so this should be enough for FeS_2 pyrite formation. It is a well known problem, however, that FeS_2 can easily lose the sulfur and can be transformed into a series of FeS_{2-x} compounds. In [2] the problem is solved by an excess of partial pressure of TBDS over $Fe(CO)_5$ (see table 3). So, practically, iron atoms are deposited in a sulfur atmosphere [2]. The post-deposition XRD analysis revealed the relative content of marcasite and pyrite phases and their dependence on the growing temperature (see figure 14). As can be seen, only for deposition temperatures above 525 °C can the pure pyrite phase be obtained. So far the phase diagram for the Fe–S system is not well established, but in [26] it was shown that FeS_2 pyrite thin films can be prepared by a double source vacuum vapour deposition technique at the S/Fe flux ratio in the range 6.8–14.8 and temperature >573 K.

4. Concluding remarks

These few examples clearly demonstrate the capability of the MOCVD technique as well as the capability of the use of complex compounds for the synthesis of practically relevant thin films of oxides and sulfides. The development of compounds with three or more elements in a molecule is certainly promising. For example, the complex compounds $(Ph_3P)_2CuIn(XR)_4$ (R = Et, X = S, Se; R = *iso*-Bu, X = S) [27], where the fragments $(Ph_3P)_2Cu$ and $In(XR)_2$ are bonded, were synthesized. The decomposition of these compounds leads to $CuInS_2$ or $CuInSe_2$ materials.

Acknowledgments

Part of the work described was supported by Fundação para a Ciência e Tecnologia projects POCTI/43520/FIS/2000, 423/DAAD-ICCTI and by project II-01-64 (HASYLAB).

References

[1] Vescan L 1995 *Handbook of Thin Film Process Technology* B1.0:1 (Bristol: Institute of Physics Publishing)
[2] Höpfner C, Ellmer K, Ennaoui A, Pettenkofer C, Fiechter S and Tributsch H 1995 *J. Cryst. Growth* **151** 325–34
[3] Battiston G A, Carta G, Cavinato G, Gerbasi R, Porchia M and Rossetto G 2001 *Chem. Vapor Depos.* **7** 69–74
[4] Krumdieck S P and Rai R 2001 *Chem. Vapor Depos.* **7** 85–90
[5] Tanpipat N, Andzelm J, Delley B, Korkin A and Demkov A 2000 *Proc. 15th Int. Symp. on Chemical Vapour Deposition (Toronto, Canada, 2000)* pp 1–7
[6] Amato-Wierda C C and Norton E T Jr 2000 *Proc. 15th Int. Symp. on Chemical Vapour Deposition (Toronto, Canada, 2000)* pp 84–9
[7] Bessergenev V G, Belyi V I, Rastorguev A A, Ivanova E N, Kovalevskaya Yu A, Larionov S V, Zemskova S M, Kirichenko V N, Nadolinnyi V A and Gromilov S A 1994 *Preprint* 94-02
[8] Bessergenev V G, Ivanova E N, Kovalevskaya Yu A, Gromilov S A, Kirichenko V N, Zemskova S M, Vasilieva I G, Aupov B M and Shwarz N L 1995 *Mater. Res. Bull.* **30** 1393–400
[9] Bessergenev V G, Belyi V I, Rastorguev A A, Ivanova E N, Kovalevskaya Yu A, Larionov S V, Zemskova S M, Kirichenko V N, Nadolinnyi V A and Gromilov S A 1996 *Thin Solid Films* **279** 135–9
[10] Belyi V I, Rastorguev A A, Ivanova E N, Larionov S V, Zemskova S M, Bessergenev V G and Kovalevskaya Yu A 1994 *Patent Specification* 5062316/26, Russia
[11] Belyi V I, Rastorguev A A, Ivanova E N, Larionov S V, Kirichenko V N, Bessergenev V G and Kovalevskaya Yu A 1994 *Patent Specification* 92000601/26, Russia
[12] Bessergenev V G, Ivanova E N, Kovalevskaya Yu A, Vasilieva I G, Varand V L, Zemskova S M, Larionov S V, Kolesov B A, Aupov B M and Logvinenko V A 1997 *Mater. Res. Bull.* **32** 1403–10
[13] Bessergenev V G, Ivanova E N, Kovalevskaya Yu A, Gromilov S A, Kirichenko V N and Larionov S V 1996 *Inorg. Mater.* **32** 592–6
[14] Bessergenev V G, Bessergenev A V, Ivanova E N and Kovalevskaya Yu A 1998 *J. Solid State Chem.* **137** 6–11
[15] Krisyk V V, Turgambaeva A E, Igumenov I K, Bessergenev V G, Khmelinskii I V and Pereira R J F 2000 *Proc. 15th Int. Symp. on CVD (Toronto, Canada, 2000)* pp 284–91
[16] Bessergenev V G, Khmelinskii I V, Pereira R J F, Krisuk V V, Turgambaeva A E and Igumenov I K 2002 *Vacuum* **64** 275–9
[17] McClune W F (ed) 1983 *Powder Diffraction File, International Centre of Diffraction Data, Cards* N5–492, 5–566 JCPDC, PA
[18] Swiatek K, Goldewski M, Hommel D and Hartmann H 1989 *Phys. Status Solidi* a **114** 127
[19] Brown M R and Shand W A 1970 *J. Mater. Sci.* **5** 790
[20] Vasilyeva I G, Malakhov V V, Vlasov A A and Predtechensky M R 1997 *Thin Solid Films* **292** 85
[21] Shelpakova I R, Yudelevich I G and Ayupov B M 1984 *Layer by Layer Analysis of Electronic Materials* (Novosibirsk: Nauka) p 158
[22] Nilsen W G 1969 *Phys. Rev.* **182** 838
[23] Arguello C A, Rousseau D L and Porto S P S 1969 *Phys. Rev.* **181** 1351
[24] Schlegel A and Wachter P 1973 *Solid State Commun.* **13** 1865
[25] Adams D M 1974 *Inorganic Solids* (New York: Wiley) p 72
[26] Sasaki S, Sugii A and Ishii K 1999 *J. Mater. Sci. Lett.* **18** 1193
[27] Hirpo W, Dhingra S, Sutorik A C and Kanatzidis M G 1993 *J. Am. Chem. Soc.* **115** 1597
[28] Rogalsky M S, Bessergenev V G, Barata N R A and Baltazar R 2003 *IEEE Trans. Mag.* **39** 2696